An Analysis of the Effects of $^1H^N-^1H^N$ Dipolar Couplings on the Measurement of Amide Bond Vector Orientations in Invisible Protein States by Relaxation Dispersion NMR

Hugo van Ingen, Dmitry M. Korzhnev, and Lewis E. Kay*

Departments of Molecular Genetics, Biochemistry and Chemistry, University of Toronto, Toronto, Ontario, Canada, M5A 1A8

Received: March 27, 2009; Revised Manuscript Received: May 20, 2009

Marginally and transiently populated conformational states of biomolecules can play important functional roles in biochemical processes. It is of significant interest, therefore, to develop tools for characterizing the structural and dynamical properties of these excited states. One recent development has been the emergence of spin-state-selective relaxation dispersion methods for quantifying dipolar vector orientations in invisible excited-state conformers through measurement of residual dipolar couplings (RDCs). Particularly powerful are $^1H^N-^{15}N$ RDCs that can be measured with high sensitivity on fractionally aligned, deuterated, uniformly ^{15}N-labeled protein samples. Fractional alignment also produces nonzero $^1H^N-^1H^N$ dipolar couplings. These can be problematic for the extraction of robust $^1H^N-^{15}N$ RDC values, and hence amide bond vector orientations, in cases where the amide proton of interest and a proximal amide proton have small chemical shift differences and a significant $^1H^N-^1H^N$ dipolar coupling. Here, we show that while this strong coupling effect leads to aberrant relaxation dispersion profiles, extracted excited-state $^1H^N-^{15}N$ RDCs are for the most part only marginally affected. Experimental examples of such aberrant profiles are provided, as well as a theoretical consideration of the influence of this strong coupling effect and numerical simulations that assess its impact on extracted parameters.

Introduction

Important biochemical processes such as catalysis, ligand binding, and protein folding often involve conformational states of biomolecules that are only marginally populated as functional intermediates.[1−5] An understanding of these processes requires, therefore, quantitative studies of the structural and dynamical features of these excited states, at a level of detail that is normally reserved for the dominant ground-state conformation. Unfortunately, many biochemically important excited states cannot be detected due to their low abundance and transient nature, precluding their analysis. NMR spectroscopy provides a unique opportunity to characterize these states indirectly, provided that the excited state interconverts with the ground state on a time scale of micro- to milliseconds.[6] Consider, for example, a system undergoing chemical exchange between two states, G (ground state) and E (excited state)

$$\mathrm{G} \underset{k_{\mathrm{EG}}}{\overset{k_{\mathrm{GE}}}{\rightleftarrows}} \mathrm{E}$$

where NMR probes in each of the states have distinct chemical shifts, ω_G, ω_E (i.e., $\Delta\omega_{GE} = \omega_G - \omega_E \neq 0$). The stochastic exchange between states leads to an effective time modulation of chemical shifts so that the resulting NMR signal becomes dependent on the populations of the major (G) and minor (E) exchanging states, p_G and $p_E = 1 - p_G$ as well as $k_{ex} = k_{GE} + k_{EG}$ and $\Delta\omega$. Thus, both thermodynamic (populations) and kinetic (rates) and structural properties (chemical shift differences) of the excited state are encoded in the observed resonances that derive from the visible ground state.

The pivotal experimental method for the study of millisecond time scale exchange events is the Carr−Purcell−Meiboom−Gill (CPMG) relaxation−dispersion technique,[7,8] composed of a series of consecutive spin−echoes ($\tau-180°-\tau$) that are applied within a fixed time interval.[9,10] The stochastic modulation of chemical shifts leads to the case where in general the magnetization of each state is not completely refocused by the application of a single spin−echo. However, for exchange processes in the millisecond regime, application of increasing numbers of 180° pulses during a fixed interval of evolution leads to refocusing because the effective chemical shift difference between exchanging spins is scaled down with the number of pulses. By quantifying the magnetization that is refocused at the end of the evolution period relative to its initial value as a function of the number of refocusing 180° pulses, it is possible to extract the parameters of the exchange process mentioned above. A particularly powerful feature of the experiment is that information about the minor state, E, can be obtained even in cases where E is "invisible", so long as it is populated to approximately 0.5%.[6] Combined analysis of data sets recorded at multiple magnetic field strengths and multiple temperatures and for multiple probes allows robust, accurate, and detailed characterization of the energy landscape that drives the exchange process including activation enthalpies and entropies.[3,11] Most importantly, it is also possible to extract structural information in the form of chemical shifts and currently there are protein-based experiments for measuring backbone shifts of $^{13}C^{\alpha}$, ^{13}CO, ^{15}N, $^1H^N$, and $^1H^{\alpha}$ nuclei.[9,10,12−16]

Recently, spin-state-selective relaxation dispersion experiments have been developed for the measurement of residual dipolar couplings (RDCs) in the excited state.[17−19] RDCs are exquisitely sensitive to the orientation of dipolar interaction vectors with respect to a molecule-fixed frame[20,21] and hence provide valuable structural information that complements that generated from chemical shifts. Indeed, the combined measure-

* Corresponding author. Phone: +1-416-978-0741. Fax: +1-416-978-6885. E-mail: kay@pound.med.utoronto.ca.

10.1021/jp902793y CCC: $40.75
Published on Web 07/01/2009

ment of RDCs and chemical shifts of the excited state provides an avenue for the determination of structures of these invisible conformers at a level of detail that until now has been reserved only for applications involving ground-state conformations of proteins.[22] Of course, the determination of accurate structures depends critically on the measurement of accurate parameters. Extraction of accurate RDC values is predicated on the fact that modulation of the echo amplitude occurs only due to the chemical exchange event of interest and is not the result of other interactions. It is well-known, however, that scalar spin−spin interactions can cause spin−echo amplitude modulations,[23] which are usually avoided in relaxation dispersion studies of biomolecules by using the proper labeling scheme or experimental design that removes or suppresses the appropriate couplings.[13−16,24−26] In the case of studies measuring RDC values, relaxation dispersion experiments are performed on aligned samples and "unwanted" dipolar couplings can be generated that interfere with the measurement. For example, consider the measurement of $^1H^N-^{15}N$ RDC values, and hence amide bond vector orientations, in invisible excited protein states. This is achieved by recording relaxation dispersion profiles of TROSY and anti-TROSY components of ^{15}N magnetization.[17] Significant nonzero $^1H^N-^1H^N$ RDCs can be expected,[27] and, depending on the chemical shift difference between the coupled amide protons, this can result in strong coupling that modulates the ^{15}N dispersion profiles of TROSY and anti-TROSY magnetization. Here we examine this effect in detail. Initially, a theoretical description of strong dipolar coupling is provided along with guidelines for when such effects can be significant. Subsequently, the influence of $^1H^N-^1H^N$ RDCs on ^{15}N relaxation dispersion profiles is discussed, followed by simulations that estimate the errors in measured $^1H^N-^{15}N$ RDC values as a function of the strength of the $^1H^N-^1H^N$ coupling. It is shown that for differences in chemical shifts between the dipolar coupled amide protons of greater than 0.1 ppm only relatively small errors in extracted $^1H^N-^{15}N$ RDCs are generated, typically well under 1 Hz.

Materials and Methods

NMR Spectroscopy. NMR experiments were performed on a perdeuterated, uniformly ^{15}N labeled L24A mutant of the FF domain of HYPA/FBP11[28−30] that was prepared as described previously.[31] Single-quantum[32] CW, TROSY and anti-TROSY[17] relaxation dispersion profiles were recorded at 20 °C and 11.7 T magnetic field strength on a sample aligned in a polyethyleneglycol/hexanol liquid crystalline phase[33] (43 Hz D_2O splitting). A constant-time CPMG interval, T_{relax}, set to 40 ms was used along with ν_{CPMG} values of 25, 50, 75, 100, 125, 150, 175, 200, 250, 300, 350, 400, 450, 500, 600, 700, 800, 900, and 1000 Hz. Measured $^1H^N-^{15}N$ RDC values of the visible ground state of the FF domain corresponding to the folded form of the molecule ranged from −35 to +26 Hz; these values were used along with a NMR structure of the domain[28] refined using multiple RDC data sets (unpublished data) to calculate an alignment tensor with $A_a = 12.9 \times 10^{-4}$ and $A_r = -3.9 \times 10^{-4}$ from which subsequently all $^1H^N-^1H^N$ residual dipolar couplings were predicted using the program REDCAT.[34]

Numerical Simulations. The effect of strong AB coupling on spin−echo-based experiments was evaluated using numerical simulations of the evolution of a 4-spin system composed of pairs of $^1H^N-^{15}N$ spin systems linked by the residual dipolar interaction between the $^1H^N$ protons. Simulations in the absence of exchange and neglecting pulse imperfections were performed using the open source computing language GNU Octave (http://www.gnu.org/software/octave/) by solving the Liouville−von Neumann equation describing the evolution of the density matrix in a 16 × 16-dimensional space spanned by the direct products of the Zeeman spin states for the four spins.[35] Simulations including two-site exchange and relaxation were performed using MATLAB (MathWorks, Inc.) in a 512-dimensional operator space spanned by the 256 Cartesian product operators for the 4-spin system in each of the two exchanging sites. Evolution of the density operator was evaluated using the homogeneous Bloch−McConnell equations[36,37] for a 4-spin system, modified to include evolution due to the AB dipolar coupling interaction. To include relaxation effects, a relaxation matrix was set up for all 64 $^{15}N^{A/B}$ transverse operators for which the total coherence order is ±1 and the four $^{15}N^{A/B}$ operators corresponding to longitudinal magnetization/order: N_z^A, $2N_z^AA_z$, $2N_z^BB_z$, N_z^B (required for the longitudinal equilibration delay after the CPMG sequence[17]). The transverse operators include: N_i^A, $2N_i^AA_z$, $2N_i^AB_z$, $2N_i^AN_z^B$, $4N_i^AA_zB_z$, $4N_i^AA_zN_z^B$, $4N_i^AN_z^BB_z$, $8N_i^AA_zN_z^BB_z$, $4N_i^AA_jB_k$, $8N_i^AA_jB_kN_z^B$ where the superscripts A and B distinguish between nitrogens attached to proton spins A and B and $i, j, k \in \{x,y\}$. In the case where evolution from ^{15}N chemical shift is neglected, only 16 elements are needed that further reduces to 8 in the case where spins A and B are assumed to have the same chemical shift (see Results and Discussion). Unless indicated otherwise, the following autorelaxation rates were used for elements in both ground and excited states: $R_1(N_z^A) = 0.60\ s^{-1}$ (R_{1z}); $R_1(2N_z^AA_z) = 4.0\ s^{-1}$ (R_{1zz}); $R_2(N_i^A) = 18\ s^{-1}$ (at 500 MHz)/23 s^{-1} (at 800 MHz) (R_2); $R_2(2N_i^AA_z) = R_2 + (R_{1zz} - R_{1z})$; $R_2(2N_i^AB_z) = R_2 + (R_{1zz} - R_{1z})$; $R_2(2N_i^AN_z^B) = R_2 + R_{1z}$; $R_2(4N_i^AA_zB_z) = R_2 + 2(R_{1zz} - R_{1z})$; $R_2(4N_i^AA_zN_z^B) = R_2 + (R_{1zz} - R_{1z}) + R_{1z}$; $R_2(4N_i^AN_z^BB_z) = R_2 + (R_{1zz} - R_{1z}) + R_{1z}$; $R_2(8N_i^AA_zN_z^BB_z) = R_2 + 2(R_{1zz} - R_{1z}) + R_{1z}$; $R_2(4N_i^AA_jB_k) = R_2 + 5(R_{1zz} - R_{1z})$; $R_2(8N_i^AA_jB_kN_z^B) = R_2 + 5(R_{1zz} - R_{1z}) + R_{1z}$, where the proton spins are assumed to relax only from external protons, with the transverse relaxation rate of a proton spin a factor of 2.5 larger than its longitudinal relaxation rate;[38] the factor of 5 in some of the above expressions derives from the fact that there are a pair of transverse ^1H spins (A and B), each contributing $2.5(R_{1zz} - R_{1z})$ to the relaxation rate. Cross-relaxation caused by cross-correlated interactions between the ^{15}N CSA and $^1H-^{15}N$ dipolar relaxation mechanisms was explicitly included. Transverse cross-relaxation was included between the following pairs: $\{N_i^A, 2N_i^AA_z\}$, $\{2N_i^AB_z, 4N_i^AA_zB_z\}$, $\{4N_i^AN_z^BB_z, 8N_i^AA_zN_z^BB_z\}$ and $\{2N_i^AN_z^B, 4N_i^AA_zN_z^B\}$. The longitudinal cross-relaxation rate η_z was set to 0.16 s^{-1}, the transverse rate η_{xy} was set to 11.5 s^{-1} (both at 500 MHz; η_{xy} (η_z) scaled linearly (inversely) with field for simulations at 800 MHz). Identical relaxation rates were assumed for the N^B subspace. All rates are those measured for T4 lysozyme at 20 °C (correlation time ∼12 ns). Additional simulations were performed using relaxation parameters for the FF domain (correlation time ∼4 ns; data not shown). All simulations assumed perfect pulses and neglected off-resonance effects.

To determine the accuracy of extracted excited-state RDCs in the case where nonzero $^1H^N-^1H^N$ residual dipolar couplings (D_{HH}) are present, dispersion profiles were simulated for ^{15}N TROSY, anti-TROSY, and CW-SQ magnetization at field strengths of 11.7 and 18.8 T using the following parameters: $T_{relax} = 40$ ms, $\nu_{CPMG} = 25$, 50, 75, 100, 125, 150, 175, 200, 225, 250, 300, 350, 400, 450, 500, 600, 700, 800, 900, and 1000 Hz, $D_{HH,ground} = D_{HH,excited}$, $p_E = 5\%$, $\Delta\varpi_{N,GE} = 2$ ppm and $k_{ex} = 500\ s^{-1}$ for several values of D_{HH} and ΔD_{NH} (difference between $^1H-^{15}N$ RDCs in the ground and excited states) with AB chemical shift differences between 0 and 0.5

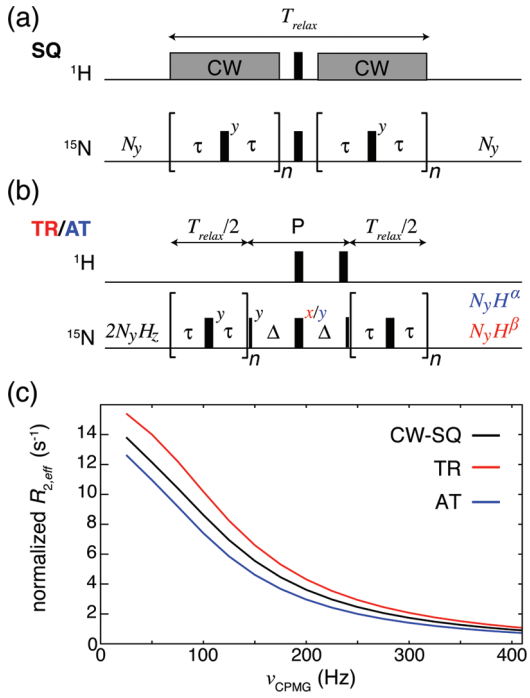

Figure 1. CPMG relaxation dispersion schemes and resultant dispersion profiles from which excited-state $^1H^N-^{15}N$ RDCs are extracted. Constant-time CPMG elements are shown for measuring (a) ^{15}N single-quantum (SQ) relaxation dispersion profiles with continuous-wave (CW) ^1H decoupling and (b) ^{15}N TROSY/anti-TROSY (TR/AT) dispersion profiles. The P-element exchanges antiphase and in-phase magnetization while preserving the ^1H spin state.[17,39] (c) Schematic normalized dispersion profiles ($R_{2,eff}(\nu_{CPMG}) - R_{2,eff}(\nu_{CPMG} \rightarrow \infty)$) for a case where ΔD_{NH} is nonzero.

ppm. For each parameter set, 50 Monte Carlo sets were generated by adding Gaussian distributed noise with a standard deviation of 0.4 s^{-1} to the calculated $R_{2,eff}$ values. Each of the 50 sets (6 simulated dispersion profiles per set, including TROSY, anti-TROSY, and CW-SQ at 11.7 and 18.8 T) were subsequently fitted using the fitting program CATIA (http://pound.med.utoronto.ca/software). The average fitted ΔD_{NH}, the average error in ΔD_{NH} reported by CATIA, and the average reduced χ^2 were determined from the resulting 50 fits for each set of simulated parameters.

Results and Discussion

Relaxation Dispersion NMR Experiments for Extraction of Residual Dipolar Couplings. Figure 1 illustrates two constant-time CPMG pulse train elements that form the basic building blocks of the relaxation dispersion experiments discussed in the paper. These elements can operate on in-phase magnetization, N_y (^{15}N transverse y-magnetization, referred to in what follows as SQ), as in the example of Figure 1a, or TROSY, N_yH^β (TR), or anti-TROSY, N_yH^α (AT) magnetization, as in Figure 1b, where $H^\beta(H^\alpha)$ indicates that the spin state of the amide proton one-bond coupled to the ^{15}N probe is in the $\beta(\alpha)$ state. In the TR/AT class of experiment the initial magnetization is antiphase, $2N_yH_z = (N_yH^\alpha - N_yH^\beta)$, and either the TR or AT component that is present at the completion of the CPMG pulse train is selected for.

In the case where millisecond-time scale chemical exchange is present, the effective transverse relaxation rate, $R_{2,eff}(\nu_{CPMG})$, varies with the number n of refocusing pulses applied during the fixed relaxation period, T_{relax} ($\nu_{CPMG} = n/T_{relax}$), and can be calculated according to

$$R_{2,eff}(\nu_{CPMG}) = -\frac{1}{T_{relax}}\ln\left(\frac{I(\nu_{CPMG})}{I_0}\right) \quad (1)$$

where $I(\nu_{CPMG})$ and I_0 are intensities of magnetization with and without the CPMG element. If the dispersion experiments are carried out in isotropic solution, then to within an offset the profiles produced, $R_{2,eff}(\nu_{CPMG})$, are independent of whether N_y, N_yH^α, or N_yH^β is probed. By contrast, if the experiments are performed under conditions of weak alignment each dispersion profile is distinct, Figure 1c, with the profile derived from N_y (black) in between those from N_yH^α (blue) and N_yH^β (red). It has been shown previously that these differences derive from the fact that the N_y, N_yH^α, and N_yH^β dispersion profiles are sensitive to effective chemical shift differences of $\Delta\omega$, $\Delta\omega + \Delta D_{NH}/2$ and $\Delta\omega - \Delta D_{NH}/2$, respectively, where ΔD_{NH} is the difference between $^1H-^{15}N$ residual dipolar couplings (RDCs) in the ground and excited states. Thus, by fitting the three profiles simultaneously it becomes possible to measure ΔD_{NH} values and ultimately $^1H-^{15}N$ RDCs in the invisible excited state.

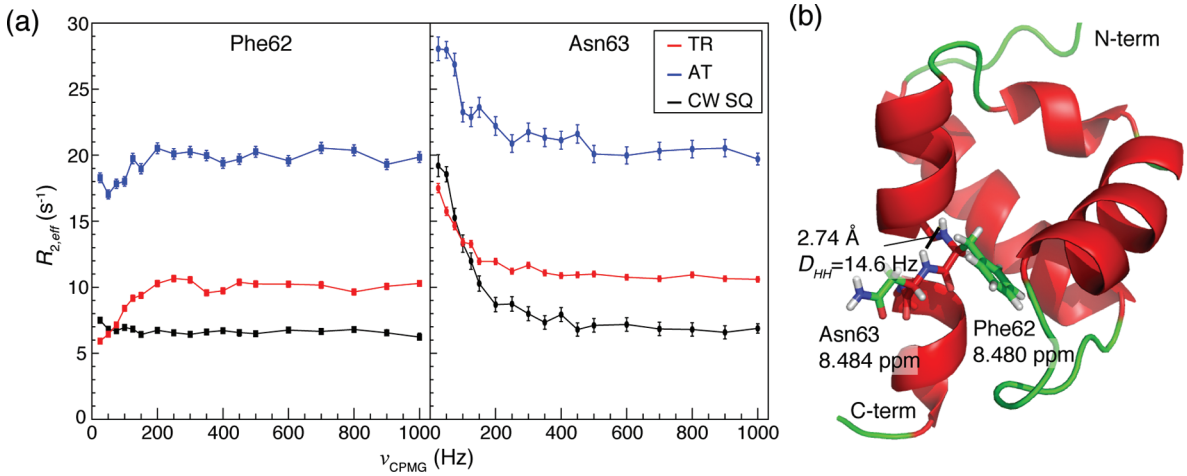

Figure 2. Strong $^1H^N-^1H^N$ coupling artifacts in TROSY/anti-TROSY CPMG relaxation dispersion experiments. (a) Experimental CPMG relaxation dispersion curves derived from SQ (black), TROSY (red), and anti-TROSY (blue) ^{15}N coherences for residues Phe62 and Asn63 of perdeuterated L24A FF domain. (b) Refined NMR structure of the wild-type FF domain,[28] indicating the short distance and the predicted $^1H^N-^1H^N$ dipolar coupling constant connecting the amide protons of residues Phe62 and Asn63.

Potential Artifacts in Spin-State-Selective Relaxation Dispersion Experiments. The spin-state-selective experiments that probe chemical exchange by quantifying the relaxation of ^{15}N TROSY and anti-TROSY magnetization components (Figure 1b) are sensitive to certain artifacts that do not affect in-phase ^{15}N transverse magnetization (Figure 1a). Consider first the case of a four-spin system consisting of two $^1H^N-^{15}N$ spin pairs where the $^1H^N$ protons are not proximal. Since the scalar coupling between the two protons is negligible and since little if any residual $^1H^N-^1H^N$ dipolar coupling is produced upon alignment (couplings scale as the cube of the inverse distance), SQ, TR, and AT dispersion profiles that are similar to those in Figure 1c would be measured. In contrast, if the $^1H^N$ protons are proximal so that a sizable $^1H^N-^1H^N$ dipolar coupling is generated upon alignment and further if the coupled $^1H^N$ protons have similar chemical shifts, then the amide protons become strongly coupled and the evolution of N_yH^α or N_yH^β during the CPMG pulse train reflects this strong coupling (see below). This can have serious consequences for the dispersion profiles, as illustrated in Figure 2a, where experimental data is presented, recorded on an FF-domain that undergoes exchange between its folded state and an "invisible" folding intermediate. The amide ^{15}N of Phe62 is relatively insensitive to this exchange process ($\Delta\varpi \approx 0.26$ ppm) since a nearly flat SQ dispersion profile is obtained (black). However, aberrant TR and AT dispersion profiles are produced that are recorded using the scheme of Figure 1b. Note that both curves increase with ν_{CPMG}, indicating elevated signal loss as a function of pulse rate. In addition, the dispersion profile generated for N_y is lower than those for N_yH^α and N_yH^β that is not in keeping with expectations (Figure 1c). The neighboring residue, Asn63, is sensitive to the exchange process, with the artifact manifested (i) as an anomalous offset between the TR, AT, and SQ profiles and (ii) as a reduced dispersion of $R_{2,eff}$ values ($R_{2,eff}$(1000 Hz) $-$ $R_{2,eff}$(25 Hz)) for the TR/AT profiles as compared to the SQ data.

A ribbon diagram of the FF domain is presented in Figure 2b, highlighting residues Phe62 and Asn63. Based on the short interatomic distance between the $^1H^N$ protons of Phe62 and Asn63 (2.74 Å) and the experimentally measured $^1H^N-^{15}N$ RDCs in the protein, a residual $^1H^N-^1H^N$ dipolar coupling, D_{HH}, of 14.6 Hz is predicted using the program REDCAT.[34] The finite value of D_{HH} and the nearly identical chemical shifts of the $^1H^N$ protons for these residues (1.6 Hz difference at 500 MHz) leads to a strongly coupled AB spin system, which produces the artifactual TR and AT dispersion profiles (see below).

A Simple Picture of the Effects of Strong $^1H^N-^1H^N$ Coupling. Figure 3a shows a pair of $^1H^N-^{15}N$ spin systems, linked by the residual dipolar interaction between the $^1H^N$ protons, that is considered in the analysis below. In the case of strong $^1H^N-^1H^N$ dipolar coupling an ABMX spin system results (with A,B and M,X the pairs of proton and nitrogen spins, respectively) and the evolution of magnetization during free precession proceeds under the Hamiltonian:

$$\hat{\mathscr{H}} = \pi(J_{NH} + D^A_{NH})2\hat{N}^A_z\hat{A}_z + \pi(J_{NH} + D^B_{NH})2\hat{N}^B_z\hat{B}_z + \pi D_{HH}(3\hat{A}_z\hat{B}_z - \vec{\mathbf{A}}\cdot\vec{\mathbf{B}}) + \Omega_A\hat{A}_z + \Omega_B\hat{B}_z + \Omega_{NA}\hat{N}^A_z + \Omega_{NB}\hat{N}^B_z \quad (2)$$

which can be rewritten as

$$\hat{\mathscr{H}} = \pi J^A_{eff}2\hat{N}^A_z\hat{A}_z + \pi J^B_{eff}2\hat{N}^B_z\hat{B}_z + \frac{1}{2}\sum\Omega(\hat{A}_z + \hat{B}_z) + \frac{1}{2}\Delta\Omega(\hat{B}_z - \hat{A}_z) + \pi D_{HH}\left(2\hat{A}_z\hat{B}_z - \frac{1}{2}\hat{A}_+\hat{B}_- - \frac{1}{2}\hat{A}_-\hat{B}_+\right) \quad (3)$$

where $\sum\Omega = \Omega_B + \Omega_A$, $\Delta\Omega = \Omega_B - \Omega_A$, $J_{eff} = J_{NH} + D_{NH}$, the superscripts A, B distinguish between nitrogens attached to proton spins A and B or effective couplings that pertain to each of the $^{15}N-^1H^N$ spin systems, and the Zeeman terms of the ^{15}N spins have been removed since they commute with all other terms and hence can be considered separately. The $\hat{A}_+\hat{B}_-$ and $\hat{A}_-\hat{B}_+$ terms that arise from the $^1H^N-^1H^N$ dipolar Hamiltonian do not commute with the J_{NH} scalar coupling Hamiltonian. These terms are important in the case of strong coupling and lead to mixing of the $|\alpha\beta\rangle$ and $|\beta\alpha\rangle$ proton spin states that are eigenfunctions of the scalar coupling Hamiltonian in the weak-coupling limit. For example, in the classical example of strong scalar coupling in a two-spin system, the eigenfunctions become

$$\begin{aligned} |\alpha\beta\rangle\cos\left(\frac{\varphi}{2}\right) + |\beta\alpha\rangle\sin\left(\frac{\varphi}{2}\right) \\ |\alpha\beta\rangle\sin\left(\frac{\varphi}{2}\right) - |\beta\alpha\rangle\cos\left(\frac{\varphi}{2}\right) \end{aligned} \quad (4)$$

where the angle ϕ is defined as $\tan(\phi) = 2\pi J/\Delta\Omega$. This angle provides a measure of the "strength" of the coupling interaction, i.e., whether the spin system is weakly ($\phi \rightarrow 0$) or strongly coupled ($\phi \rightarrow \pi/2$).[35] In the particular case of strong proton coupling in the 4-spin ABMX system considered here, both scalar coupled protons A and B are additionally coupled to their respective ^{15}N nuclei. Thus, there are four unique scenarios of (infinitely) strong coupling, depending on which lines of the proton doublet overlap. This is illustrated schematically in Figure 3b where simplified proton spectra are shown that include the $^1H^N-^{15}N$ dipolar/scalar coupling but neglect the additional lines that arise from the $^1H^N-^1H^N$ interaction. In this representation the spectrum of each $^1H^N$ is composed of a pair of lines that results from the one-bond $^1H^N-^{15}N$ coupling, with each line associated with a particular ^{15}N spin state, as depicted. The corresponding four ϕ angles are given by

$$\begin{aligned} \tan(\varphi_1) &= \frac{\pi D_{HH}}{\pi J^A_{eff} - \pi J^B_{eff} - \Delta\Omega} \\ \tan(\varphi_2) &= \frac{\pi D_{HH}}{\pi J^A_{eff} + \pi J^B_{eff} - \Delta\Omega} \\ \tan(\varphi_3) &= \frac{\pi D_{HH}}{\pi J^A_{eff} + \pi J^B_{eff} + \Delta\Omega} \\ \tan(\varphi_4) &= \frac{\pi D_{HH}}{\pi J^A_{eff} - \pi J^B_{eff} + \Delta\Omega} \end{aligned} \quad (5)$$

When any of these angles approaches $\pm\pi/2$, protons A and B become strongly coupled, resulting in mixing of the $|AB\rangle = \{|\alpha\beta\rangle, |\beta\alpha\rangle\}$ eigenstates. For example, when H^N lines that derive from N^A and N^B both in the $|\alpha\rangle$ spin-state overlap ($\phi_1 = \pi/2$, Figure 3b) the eigenfunctions become

$$\begin{aligned} |\alpha\beta\alpha\alpha\rangle \cos\left(\frac{\varphi_1}{2}\right) + |\beta\alpha\alpha\alpha\rangle \sin\left(\frac{\varphi_1}{2}\right) \\ |\alpha\beta\alpha\alpha\rangle \sin\left(\frac{\varphi_1}{2}\right) - |\beta\alpha\alpha\alpha\rangle \cos\left(\frac{\varphi_1}{2}\right) \end{aligned} \quad (6)$$

where the ket denotes the spin states of A, B, N^A, and N^B sequentially. In a similar manner, overlap of H^N lines corresponding to N^A and N^B in the $\{|\alpha\rangle, |\beta\rangle\}$, $\{|\beta\rangle, |\alpha\rangle\}$, and $\{|\beta\rangle, |\beta\rangle\}$ spin states is described by $\phi_2 = \pi/2$, $\phi_3 = \pi/2$, and $\phi_4 = \pi/2$, respectively.

The expressions of eq 5 can be used to provide relations between $\Delta\Omega$, D_{HH}, and $\pi J^A_{eff} \pm \pi J^B_{eff}$ that pertain in the strong coupling regime, leading to the appearance of artifacts in dispersion profiles, as discussed above. Typically, anomalous effects in spectra due to strong coupling emerge for $|\tan(\phi_j)| > 0.2$, $j \in \{1,2,3,4\}$, corresponding to $\Delta\Omega$ values in the range

$$\begin{aligned} -5\pi|D_{HH}| + \pi(J^A_{eff} - J^B_{eff}) < \Delta\Omega < 5\pi|D_{HH}| + \\ \pi(J^A_{eff} - J^B_{eff}) \text{ for } \tan(\varphi_1) > 0.2 \\ -5\pi|D_{HH}| + \pi(J^A_{eff} + J^B_{eff}) < \Delta\Omega < 5\pi|D_{HH}| + \\ \pi(J^A_{eff} + J^B_{eff}) \text{ for } \tan(\varphi_2) > 0.2 \\ -5\pi|D_{HH}| - \pi(J^A_{eff} + J^B_{eff}) < \Delta\Omega < 5\pi|D_{HH}| - \\ \pi(J^A_{eff} + J^B_{eff}) \text{ for } \tan(\varphi_3) > 0.2 \\ -5\pi|D_{HH}| - \pi(J^A_{eff} - J^B_{eff}) < \Delta\Omega < 5\pi|D_{HH}| - \\ \pi(J^A_{eff} - J^B_{eff}) \text{ for } \tan(\varphi_4) > 0.2 \end{aligned} \quad (7)$$

The spectra of Figure 3b illustrate the case for $|\tan(\phi_j)| = \infty$. Equation 7 establishes that by moving the relative position of the A and B ^1H spectra by ζ Hz such that $|\zeta| < |2.5D_{HH}|$, the strongly coupled situation prevails ($|\tan(\phi_j)| > 0.2$). In most applications, alignment conditions are chosen such that $|J_{NH} + D_{NH}| \approx 93 \pm 20$ Hz; with this level of alignment and assuming an $^1H^N-^1H^N$ distance of 2.4 Å (twice the ^1H van der Waals radius), a maximum D_{HH} of ≈ 15 Hz is expected so that the spin system becomes strongly coupled for $|\zeta| < 38$ Hz (0.075 ppm at 500 MHz). The effects of strong coupling are thus expected to be restricted to a relatively narrow range of frequency space that depends critically on the magnitude of D_{HH}. In what follows we consider how strong coupling influences the evolution of ^{15}N magnetization during the course of relaxation dispersion experiments.

Theoretical Description of the Effects of Strong $^1H^N-^1H^N$ Coupling in Spin−Echo-Based Experiments. As a first step toward understanding the effects of strong AB coupling on relaxation dispersion experiments we first simulated a simple ^{15}N spin−echo (τ−180°−τ) experiment as a function of both $\Delta\nu_{AB} = \Delta\Omega_{BA}/2\pi$ and the echo delay τ, assuming $D_{HH} = 10$ Hz, $J^A_{eff} = J^B_{eff} = J_{eff} = -100$ Hz (Figure 3c). There is clear modulation of the detected magnetization in both strong coupling scenarios, i.e. $\Delta\nu_{AB} = 0$ ($\phi_1 = \phi_4 = \pi/2$, Figure 3c) and for $\Delta\nu_{BA} = -J_{eff}$ ($\phi_3 = \pi/2$), with a similar modulation noted for $\Delta\nu_{BA} = J_{eff}$ ($\phi_2 = \pi/2$; not shown). For values of $\Delta\nu_{BA}$ that are in the range $\pm 2.5|D_{HH}|$, $-J_{eff} \pm 2.5|D_{HH}|$ (eq 7) the large oscillations diminish but complete refocusing of magnetization does not occur (see, for example, Figure 3c, $\Delta\nu_{BA} = 20$, 80 Hz).

In the case where $\Delta\nu_{BA} = 0$, it is possible to express the evolution of magnetization as a function of τ in relatively compact form. In this limit the equation of motion describing ^{15}N magnetization evolution under the Hamiltonian of eq 3 can be written as

$$\frac{d\vec{v}}{dt} = \tilde{\Gamma}\vec{v} \quad (8)$$

where the Liouvillian propagator matrix, $\tilde{\Gamma}$, is given by

$$\tilde{\Gamma} = \begin{pmatrix} 0 & -\pi J_{eff} & 0 & 0 & 0 & 0 \\ \pi J_{eff} & 0 & 0 & 0 & -\pi\frac{1}{2}D_{HH} & 0 \\ 0 & 0 & 0 & \pi J_{eff} & \pi\frac{1}{2}D_{HH} & 0 \\ 0 & 0 & -\pi J_{eff} & 0 & 0 & 0 \\ 0 & \pi D_{HH} & -\pi D_{HH} & 0 & 0 & -\pi J_{eff} \\ 0 & 0 & 0 & 0 & \pi J_{eff} & 0 \end{pmatrix} \quad (9)$$

and $\vec{v} = \{N^A_x, 2N^A_yA_z, 2N^A_yB_z, 4N^A_xA_zB_z, 1/2(4N^A_y(A_+B_- - A_-B_+)), 1/2(8N^A_yN^B_z(A_+B_- + A_-B_+))\}^T$, where "T" denotes transpose. Note that the total coherence order of all the operators in $\vec{v}$ is ±1.

Using eqs 8 and 9 it can be shown that starting from $2N^A_yA_z$ the fraction of this coherence, f, remaining at the completion of a single spin−echo (τ−180°−τ) in the absence of chemical exchange and neglecting relaxation is given by

$$\begin{aligned} f = \frac{1}{2} + [(D^2_{HH} + A)\cosh(\sqrt{2}\pi B_-\tau) \\ + (D^2_{HH} - A)\cosh(\sqrt{2}\pi B_+\tau)]/[4(D^2_{HH} + 4J^2_{eff})] \\ + \left[8J^2\cosh\left(\frac{1}{2}\sqrt{2}\pi B_-\tau\right)\cosh\left(\frac{1}{2}\sqrt{2}\pi B_+\tau\right)\right. \\ \left. + 4B_-B_+\sinh\left(\frac{1}{2}\sqrt{2}\pi B_-\tau\right)\sinh\left(\frac{1}{2}\sqrt{2}\pi B_+\tau\right)\right]/ \\ [4(D^2_{HH} + 4J^2_{eff})] \\ A = \sqrt{D^4_{HH} + 4D^2_{HH}J^2_{eff}} \\ B_- = \sqrt{-D^2_{HH} - 2J^2_{eff} - A} \\ B_+ = \sqrt{-D^2_{HH} - 2J^2_{eff} + A} \end{aligned} \quad (10.1)$$

that simplifies for the case $D_{HH}/J_{eff} \rightarrow 0$ to

$$\begin{aligned} f \approx \frac{1}{2} + |D_{HH}|\frac{\cosh(\sqrt{2}\pi B_-\tau) - \cosh(\sqrt{2}\pi B_+\tau)}{8J_{eff}} + \\ \frac{1}{2}\cosh\left(\frac{1}{2}\sqrt{2}(B_- - B_+)\pi\tau\right) \\ \approx \frac{1}{2} + \frac{1}{2}\cos(D_{HH}\pi\tau) \end{aligned} \quad (10.2)$$

The slow dominant oscillation with frequency $D_{HH}/4$ that is observed in Figure 3c for $\Delta\nu_{BA} = 0$ is predicted by eq 10.2. In addition, a much smaller modulation of f at a higher frequency ($\approx J_{eff}$) produces the small ripple in the curve. Notably, for the case where $\Delta\nu_{BA} = -J_{eff}$, the function $f(\tau)$ evolves at a frequency of $D_{HH}/8$.

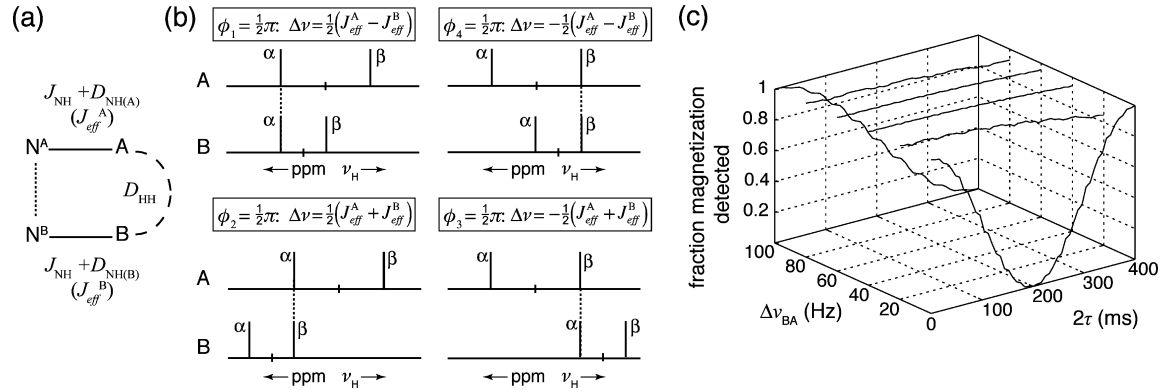

Figure 3. A qualitative picture of the four infinitely strong $^1H^N-^1H^N$ dipolar coupling scenarios. (a) Diagram of the ABMX 4-spin system considered, comprised of a pair of $^1H^N-^{15}N$ spin systems, introducing the nomenclature used throughout the paper: N^A and N^B denote two backbone ^{15}N nuclei bonded to amide protons A and B, respectively, with $J_{NH} = -93$ Hz, $0 < |D_{NH}| < 30$ Hz, and $0 < |D_{HH}| < 15$ Hz in most cases. (b) ^1H NMR "stick" spectra for protons A and B showing only the splitting of the ^1H line due to the J_{NH} scalar interaction. Note that, while the frequencies which form the numerators and denominators of eq 5 are expressed in units of radians/s, here the frequency differences, $\Delta\nu$, are expressed in Hz. (c) Fraction of ^{15}N transverse magnetization after a single spin−echo (τ−180°−τ) as function of the delay 2τ and $\Delta\nu_{BA} = (\omega_B - \omega_A)/2\pi$, the frequency offset between protons B and A, assuming no chemical exchange and no spin relaxation.

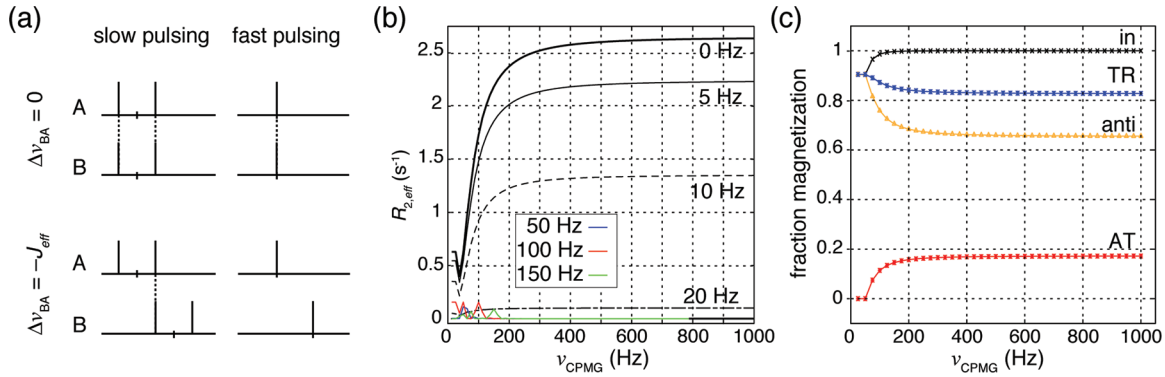

Figure 4. Effects of a strong AB ($^1H^N-^1H^N$) dipolar coupling interaction on ^{15}N-CPMG experiments. (a) ^1H stick spectra derived from spins A and B in the slow and fast pulsing limits illustrating the overlap of ^1H lines from spins A and B with $J_{eff}^A = J_{eff}^B$ (top and bottom) and with $\Delta\nu_{BA} = 0$ (top) or $-J_{eff}$ (bottom). In the slow ^{15}N pulsing regime (small ν_{CPMG} values) J_{NH} is active and the A and B lines are split as doublets, while in the fast pulsing regime J_{NH} is effectively suppressed and the A and B lines appear as singlets. In the case where $\Delta\nu_{BA} = 0$ strong coupling is present for all ν_{CPMG} values resulting in continuous magnetization loss. For $\Delta\nu_{BA} = \pm J_{eff}$ there is magnetization loss only in the slow pulsing regime where one of the A and B doublet components overlap. (b) Effective transverse relaxation rates $R_{2,eff}$ (eq 1) calculated from simulations of magnetization evolution during a CT CPMG experiment without relaxation compensation ($(\tau-180°-\tau)_N$ with $2\tau N = 40$ ms) as a function of $\Delta\nu_{BA}$, $D_{HH} = 10$ Hz. The starting/observed magnetization is antiphase ^{15}N, $2N_x^A A_z$. (c) Fraction of magnetization detected as in (b) for antiphase (orange), in-phase (black), and TROSY (blue) coherences as starting/observed magnetization, $D_{HH} = 10$ Hz. The red curve shows the amount of anti-TROSY magnetization generated at the end of the echo train when starting from pure TROSY magnetization. Simulations in (b) and (c) assume $J_{eff}^A = J_{eff}^B = -100$ Hz and neglect spin relaxation and chemical exchange.

Next, we consider a constant time (CT) ^{15}N CPMG experiment of duration T_{relax}, $(\tau-180°-\tau)_N$ with $2\tau N = T_{relax}$, in which the interpulse delay 2τ is varied at a frequency ν_{CPMG} defined according to $\nu_{CPMG} = 1/(4\tau)$; again the effects of chemical exchange and relaxation are neglected. While the ^{15}N 180° pulses of the CPMG train refocus evolution from the J_{NH} scalar interaction in the absence of strong dipolar coupling, they also effectively suppress J_{NH} scalar evolution even for the case of strong $^1H^N-^1H^N$ coupling so long as they are applied rapidly in a manner that effectively leads to spin locking of the starting magnetization. ^{15}N pulsing can also modulate how the AB dipolar interaction affects magnetization during the echo train. For example, under fast pulsing conditions and for the case where $\Delta\nu_{BA}$ is close to 0 (between $\pm 2.5|D_{HH}|$), the A and B lines effectively collapse into overlapping singlets, Figure 4a (top), so that the strong AB coupling that is present in the slow pulsing limit is also operative throughout the pulse train. By contrast, if $\Delta\nu_{BA} = -J_{eff}$ ($\phi_3 = \pi/2$), the strongly coupled situation in the slow pulsing limit is very much moderated for large ν_{CPMG} values since the A/B lines become separated in this limit, Figure 4a (bottom). Figure 4b illustrates how strong coupling can effect relaxation dispersion profiles, $R_{2,eff}(\nu_{CPMG})$, that in the present case are generated by considering the evolution of starting magnetization $2N_y^A A_z$ during a CT-CPMG spin−echo train. Because chemical exchange is not considered in these simulations, flat dispersion profiles would be expected if evolution of the starting magnetization were to be completely refocused by the CPMG pulse scheme. This is not what is observed. As the length of the constant time period T_{relax} is set to 40 ms $\ll 1/D_{HH}$, evolution under the free precession Hamiltonian of eq 3 results only in signal loss. Moreover, this signal loss occurs when the magnetization is antiphase, $2N_y^A A_z$, since the A_z component evolves due to strong $^1H-^1H$ (AB) coupling to produce other coherences that are not refocused. Signal loss does not occur when magnetization is in-phase, N_x^A, however, since pure ^{15}N magnetization does not evolve with respect to $^1H-^1H$ scalar couplings. During τ (the delay between ^{15}N 180° pulses) magnetization interchanges between $2N_y^A A_z$ and N_x^A due to evolution from J_{NH}, and the extent of magnetization loss thus becomes a function of the rate of interconversion between coherences that are susceptible to the effects of strong coupling and those that are immune. Thus, as ν_{CPMG} increases,

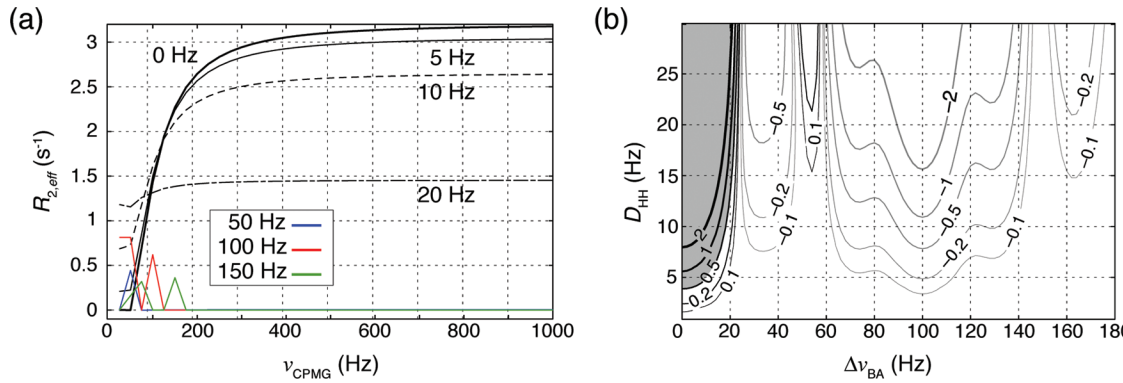

Figure 5. Effects of strong AB ($^1H^N-^1H^N$) dipolar coupling on TR/AT CPMG relaxation dispersion profiles. (a) Simulated dispersion profiles as function of the frequency offset $\Delta\nu_{BA}$, assuming $J^A_{eff} = J^B_{eff} = -100$ Hz, $D_{HH} = 10$ Hz, $T_{relax} = 40$ ms and neglecting relaxation or exchange effects. Profiles are based on the pulse scheme of Figure 1b. (b) Contour plot of $R_{2,eff}(1000\text{ Hz}) - R_{2,eff}(25\text{ Hz})$ as function of D_{HH} and $\Delta\nu_{BA}$ for $T_{relax} = 40$ ms. The area shaded in gray corresponds to the region where aberrant upward curving dispersion profiles occur (as in panel a, black profiles); in the nonshaded area the artifact is manifested by small modulations of $R_{2,eff}$ in the slow pulsing regime (as in panel a, red, green, blue profiles).

the interchange between $2N^A_yA_z$ and N^A_x becomes less frequent (i.e., the effective J_{NH} decreases), magnetization becomes spin-locked as $2N^A_yA_z$ (since this is the starting magnetization), and losses are maximal. $R_{2,eff}(\nu_{CPMG})$ therefore increases rapidly with ν_{CPMG} so long as $\Delta\nu_{BA}$ is small (see Figure 4b with $\Delta\nu_{BA} = 0$ Hz). At increasing offsets the $R_{2,eff}$ plateau becomes progressively smaller and is reduced to nearly zero at $\Delta\nu_{BA} = 20$ Hz. At higher offsets between the two proton chemical shifts, there are small modulations of $R_{2,eff}$ in the slow pulsing regime that are largest for $\Delta\nu_{BA} = 100$ Hz ($-J_{eff}$) that fulfills the strong-coupling condition in the limit of infrequent pulses (Figure 4a, bottom panel). It is worth noting that if the initial magnetization were of the form N^A_y then $R_{2,eff}(\nu_{CPMG})$ curves would be generated with exactly the opposite profile; that is, $R_{2,eff}$ would decrease with increasing ν_{CPMG}. In the limit of very rapid pulsing the magnetization would be spin-locked as in-phase and $R_{2,eff}(\nu_{CPMG})$ would be completely independent of the strong-coupling effect. The preceding discussion establishes that in-phase and antiphase magnetization components are affected differentially by strong $^1H^N-^1H^N$ scalar coupling. This differential effect on N^A_y and $2N^A_yA_z$ leads to the interconversion between TROSY and anti-TROSY components, averaging out differences in TR/AT dispersion profiles that report on $^1H-^{15}N$ RDCs, in a manner which is analogous to the effects of external protons spins ("spin flips") which also leads to averaging.[17] Starting from pure TROSY magnetization, therefore, these strong coupling induced spin-flips will produce anti-TROSY magentization, as can be seen in Figure 4c. This effect will be considered in more detail below. Thus, while the manifestations of strong coupling are somewhat different depending on the initial magnetization conditions (in-phase or antiphase), nonflat dispersion profiles are always produced that in principle could lead to the measurement of artifactual values of $^1H-^{15}N$ RDCs in the excited state (see below).

Strong AB Coupling in the TROSY/Anti-TROSY CPMG Experiment. As described above, excited-state $^1H-^{15}N$ RDCs are derived from simultaneous fits of SQ, TR, and AT dispersion data that are acquired with the pulse schemes of Figure 1a,b. It is worth noting that the SQ scheme employs a ^1H CW decoupling element, ensuring that only in-phase magnetization—that is immune to the effects of strong coupling—is present throughout the CPMG pulse train. By contrast, TR and AT dispersions profiles are affected by D_{HH}, Figure 4c, at least when simple $(\tau-180°-\tau)_N$ pulse trains are employed. In what follows we examine the evolution of magnetization during the TR/AT scheme of Figure 1b starting from $2N^A_yA_z$ and selecting either the TR or AT component at the end of the pulse train, as is done in experiments. Note that a relaxation compensated pulse scheme is employed in which two CPMG periods are separated by a so-called P-element[17,39] that converts antiphase to in-phase magnetization while preserving the proton spin state. This element was developed to minimize the net interconversion between TROSY and anti-TROSY multiplet components that results, for example, from cross-relaxation between the amide proton spin directly coupled to the nitrogen of interest and proximal proton spins.[39] It has been shown that the P-element ensures that the average amount of antiphase/in-phase magnetization is independent of the pulsing rate[39] so that, in principle, a constant signal loss due to strong coupling might be expected (i.e., flat dispersion profiles that are simply elevated relative to the case where $D_{HH} = 0$). This behavior is confirmed in our simulations (data not shown). However, unlike the original P-element that was developed for studies in isotropic solution,[39] the P-element employed here includes two flanking 90° ^{15}N pulses that compensate for the mismatch between J_{eff} and Δ (Figure 1b) since the desired relation $\Delta = 1/(4J_{eff})$ is clearly not achieved for all amide sites.[17] Interestingly, these pulses purge many of the terms that are created by evolution due to strong dipolar coupling during the first $T_{relax}/2$ period thereby "resetting" the boundary conditions for the second CPMG period. As a result, flat dispersion profiles are not produced, as can be seen in Figure 5a, where $R_{2,eff}(\nu_{CPMG})$ curves are plotted for several $\Delta\nu_{BA}$ offsets, again neglecting the effects of chemical exchange and relaxation. As with the simple $(\tau-180°-\tau)_N$ scheme considered above, $\Delta R_{2,eff}(1000\text{ Hz}) = R_{2,eff}(1000\text{ Hz}) - R_{2,eff}(25\text{ Hz}))$ is maximum for $\Delta\nu_{BA} = 0$ and becomes progressively smaller for increasing offsets. For offsets beyond approximately 20−30 Hz the major effect is modulation of $R_{2,eff}$ in the slow pulsing regime that is most pronounced for $\Delta\nu_{BA} = -1/2(J^A_{eff} + J^B_{eff})$ ($\phi_3 = \pi/2$; $\Delta\nu_{BA} = 100$ Hz in the present example; Figure 5a, red curve). Figure 5b plots $\Delta R_{2,eff}$ as a function of $\Delta\nu_{BA}$ and D_{HH}; for practical D_{HH} values (≤ 15 Hz) significant artifacts are only expected within the narrow offset range highlighted in gray and for $\Delta\nu_{BA} = -1/2(J^A_{eff} + J^B_{eff}) = 100$ Hz when $D_{HH} > 10$ Hz.

Effects of Strong AB Coupling on Dispersion Profiles of an Exchanging Spin System. To this point in our discussion we have considered the effects of strong $^1H^N-^1H^N$ dipolar coupling on the evolution of magnetization during CPMG pulse trains in the case where chemical exchange has been neglected.

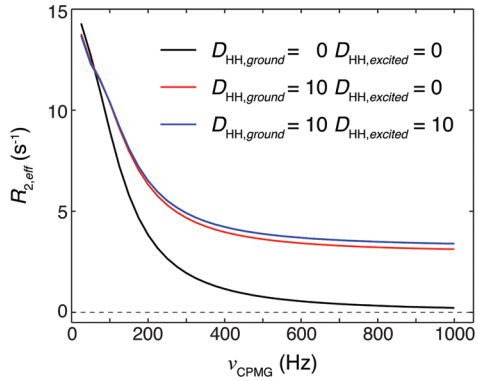

Figure 6. Effects of strong AB ($^1H^N-^1H^N$) dipolar coupling on TROSY/anti-TROSY relaxation dispersion curves that include chemical exchange and neglect spin relaxation. All profiles were simulated assuming $T_{relax} = 40$ ms, $p_E = 5\%$, $\Delta\omega_{N,GE} = 2\pi \times 100$ s^{-1}, $k_{ex} = 500$ s^{-1}, $D_{NH(A)} = D_{NH(B)} = 0$ for both ground and excited states and $\Delta\nu_{BA} = 0$ Hz. The black curve shows the dispersion profile for $D_{HH} = 0$, while red and blue curves were generated with $D_{HH,ground} = 10$ Hz and $D_{HH,excited} = 0$, 10 Hz, respectively.

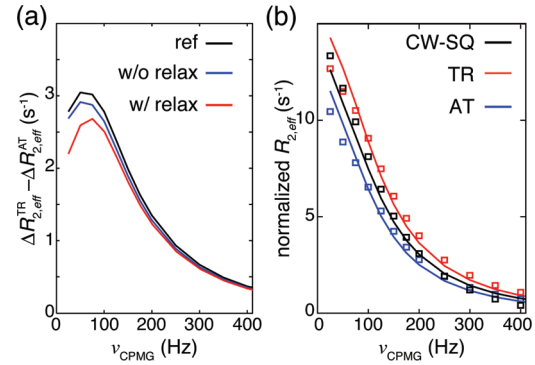

Figure 7. Combination of relaxation and strong dipolar coupling can lead to significant distortions in TR/AT dispersion profiles. (a) Plot of $\Delta R^{TR}_{2,eff} - \Delta R^{AT}_{2,eff}$ ($\Delta R_{2,eff} = R_{2,eff}(\nu_{CPMG}) - R_{2,eff}(1000$ Hz)) in the absence (black) or presence (blue and red) of strong $^1H^N-^1H^N$ dipolar coupling, either excluding (blue) or including (red) the effects of differential TROSY/anti-TROSY relaxation. Simulation parameters: $T_{relax} = 40$ ms, $p_E = 5\%$, $\Delta\omega_{N,GE} = 2\pi 100$ s^{-1}, $k_{ex} = 500$ s^{-1}, $D_{NH(A),ground} = +16$ Hz, $D_{NH(A),excited} = -4$ Hz, $D_{NH(B),ground} = D_{NH(B),excited} = 0$ Hz, $D_{HH,ground} = D_{HH,excited} = 10$ Hz and $\Delta\nu_{BA} = 0$ Hz. In the case where relaxation was considered, $\eta_{xy} = 7.5$ s^{-1} (see text). Spin flips were not included. (b) Simulated data (squares) and fits (solid lines) for the TROSY (red), anti-TROSY (blue), and CW-SQ (black) dispersion profiles $\Delta R_{2,eff}$ that were obtained using the parameters in (a), including relaxation. The three curves were fit simultaneously using in-house-developed software that does not include the effects of strong AB coupling with p_E and k_{ex} fixed to their simulated values. The reduced χ^2 of the fit was 6.0 (assuming $\sigma = 0.2$ s^{-1}), and the fitted parameters were $\Delta\omega_{N,GE} = 2\pi \times 91.7$ s^{-1} and $\Delta D_{NH} = D_{NH(A),ground} - D_{NH(A),excited} = 17.8$ Hz.

In what follows, TR and AT relaxation dispersion profiles have been simulated for the four spin system highlighted in Figure 3a that now exchanges between a dominant ground conformation and an excited state. While artifacts from strong coupling are easily recognized when there is no exchange, in the presence of exchange dispersion curves are generated that at first appearance look normal (Figure 6). To a reasonable approximation the $R_{2,eff}(\nu_{CPMG})$ dispersion curve is given by the sum of the profiles generated from strong AB coupling in the absence of exchange and from exchange in the case where $^1H^N-^1H^N$ dipolar coupling is neglected; thus, when both effects are considered together dispersion curves are produced that are of smaller magnitude and that are offset (Figure 6, red and blue profiles) relative to the case where $D_{HH} = 0$ (black). It is of interest to examine how a nonzero value of D_{HH} in the excited state might influence the dispersion profiles. Figure 6 compares $R_{2,eff}(\nu_{CPMG})$ computed with $D_{HH} = 10$ Hz, 0 Hz in the ground and excited states (red), respectively, with the profile generated with $D_{HH} = 10$ Hz, 10 Hz (blue). Only a small difference is noted corresponding to an increase in $R_{2,eff}(\nu_{CPMG})$ in the fast pulsing regime by approximately 0.3 s^{-1} in the case where a nonzero D_{HH} in the excited state is assumed. Similar small differences are noted for other exchange parameters as well.

Prior to considering a detailed simulation correlating errors in extracted $^1H^N-^{15}N$ RDC values as a function of $\Delta\nu_{BA}$ and D_{HH} we were interested in establishing how D_{HH} affects the differences between TR and AT dispersion profiles since this difference is essentially what determines the extracted ΔD_{NH} value and hence the dipolar coupling of the excited state. Figure 7a plots $\Delta R^{TR}_{2,eff} - \Delta R^{AT}_{2,eff}$ ($\Delta R_{2,eff} = R_{2,eff}(\nu_{CPMG}) - R_{2,eff}(1000$ Hz)) for the case where $D_{HH} = 0$ (ref, black) and where $D_{HH} = 10$ Hz in both ground and excited states with (red) or without spin relaxation (blue). For the case where spin relaxation is included, a value of the transverse $^1H^N-^{15}N$ dipole/^{15}N CSA cross-relaxation rate, $\eta_{xy} = 7.5$ s^{-1} was chosen that roughly corresponds to what is obtained experimentally for a protein tumbling with a 7.5 ns correlation time (500 MHz). We have purposefully not included spin flips in the present calculation since these exchange TROSY and anti-TROSY magnetization components in a manner similar to what occurs from strong $^1H^N-^1H^N$ dipolar coupling (see above) and our goal was to evaluate the influence of strong coupling, isolated from other effects (but see below). Figure 7a shows that the difference between TR and AT dispersion profiles ($\Delta R^{TR}_{2,eff} - \Delta R^{AT}_{2,eff}$) depends little on whether there is strong dipolar coupling ($D_{HH} = 10$ Hz, $\Delta\nu_{BA} = 0$ Hz in this example) so long as $\eta_{xy} = 0$ s^{-1} (compare black and blue curves) but that differences in relaxation rates between TROSY and anti-TROSY magnetization components can produce significant deviations, at least in the case of strong coupling (compare black and red profiles). Figure 7b shows SQ, TR and AT dispersion curves that have been generated with $\eta_{xy} = 7.5$ s^{-1}, $D_{HH} = 10$ Hz, $\Delta\nu_{BA} = 0$ Hz fit simultaneously using in-house software (CATIA) that does not include strong $^1H^N-^1H^N$ coupling (solid lines). It is clear that the quality of the fit is poor although the extracted ΔD_{NH} value is in error by only 11% (17.8 vs 20 Hz).

Errors in the Determination of ΔD_{NH} Resulting from Finite D_{HH} Values. In order to establish the accuracy with which ΔD_{NH} can be determined from fits of SQ, TR, and AT relaxation dispersion profiles in cases where strong $^1H^N-^1H^N$ dipolar coupling is present and to establish guidelines as to when error-free values of dipolar couplings can be extracted, we have performed extensive simulations by varying $\Delta\nu_{BA}$, D_{HH}, and k_{ex}, assuming a two-state exchanging spin system with $p_E = 5\%$ and $\Delta\varpi_{N,GE} = 2$ ppm. Simulations were carried out at two static magnetic field strengths corresponding to ^1H frequencies of 500 and 800 MHz. Values of D_{HH} and D_{NH} used in the simulations for both ground and excited states as well as all of the relaxation parameters for the density elements in the simulation are listed in Materials and Methods. The relaxation parameters used are those from measurements on T4 lysozyme, a 164-residue protein (19 kDa, correlation time ≈12 ns at 23 °C) that we are currently studying. In the simulations we have used a value of $T_{relax} = 40$ ms (see Figure 1) that is longer than optimal experimentally for a protein the size of T4 lysozyme ($T_{relax} = 25$ ms was used in experiments) because we have found that the errors from D_{HH} increase with T_{relax}; thus errors reported here can be taken as upper bounds for what might be expected from experiment.

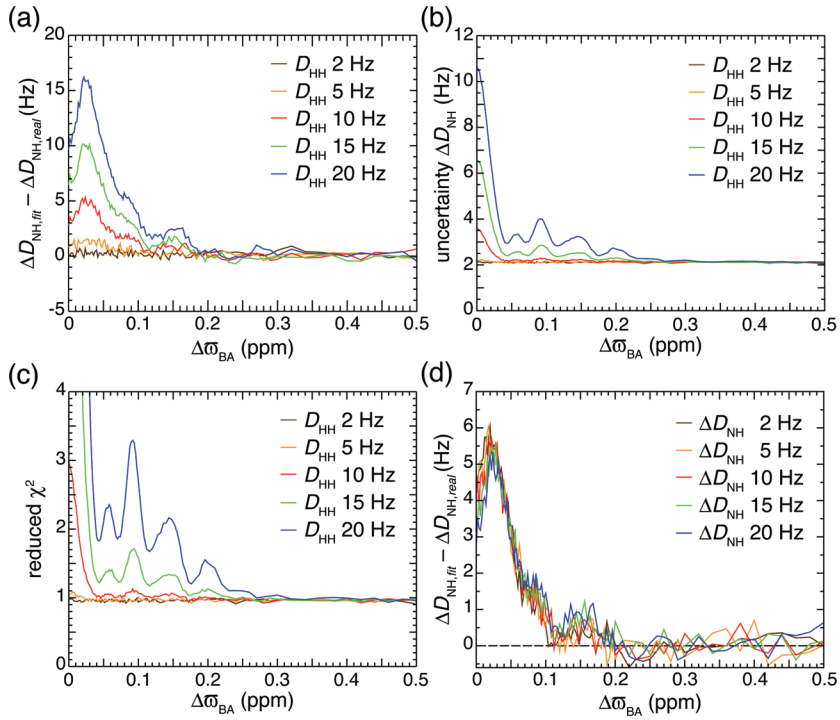

Figure 8. Accuracy of extracted excited-state $^1H^N-^{15}N$ RDC values as function of the $^1H^N-^1H^N$ chemical shift offset. Assuming $\Delta D_{NH} = 20$ Hz and relaxation parameters as for T4 lysozyme, the deviation of fitted ΔD_{NH} from the actual ΔD_{NH} value (a), the uncertainty in ΔD_{NH} as reported by the fitting program CATIA (b), and the reduced χ^2 of the resulting fits are plotted for several values of D_{HH} (c). (d) Errors of the fitted ΔD_{NH} for several values of ΔD_{NH} assuming $D_{HH} = 10$ Hz. Simulation details are given in Materials and Methods.

For each SQ, TR, and AT set of dispersion profiles generated in simulations, an additional 50 profiles were constructed with random noise, and these 50 were subsequently fitted using the program CATIA that assumes $D_{HH} = 0$. Figure 8a shows the absolute error in ΔD_{NH} as a function of $\Delta\varpi_{BA}$ (ppm) for different D_{HH} values averaged over the 50 random data sets; it is clear that for $\Delta\varpi_{BA} > 0.1$ ppm systematic errors in ΔD_{NH} do not exceed $\approx$2 Hz and are generally much smaller, even for unreasonably large values of D_{HH}. Importantly, for this offset range the systematic error in ΔD_{NH} is less than the uncertainty in ΔD_{NH} reported by CATIA (Figure 8b). In particular, the data at high offsets, where the strong coupling artifact is not present, establish that the uncertainty in ΔD_{NH} due to random errors is $\sim$2 Hz under the specific conditions chosen for the simulations. Figure 8c illustrates that the reduced χ^2 value obtained for the fit can be used as a guide to identify anomalous dispersion profiles and hence erroneous ΔD_{NH} values, assuming that the standard errors in the $R_{2,eff}$ values can be reliably estimated. Differences in fitted ($\Delta D_{NH,fit}$) and exact values ($\Delta D_{NH,real}$) of ΔD_{NH} as a function of $\Delta\varpi_{BA}$ and $\Delta D_{NH,real}$ are shown in Figure 8d, where it is clear that systematic errors in ΔD_{NH} under $\sim$1 Hz are obtained so long as $\Delta\varpi_{BA} > 0.1$ ppm (assuming $D_{HH} \leq$ 10 Hz). Finally, although changes in the exchange parameters p_E, k_{ex}, and $\Delta\varpi_{N,GE}$ will obviously affect the magnitude of the observed dispersion profiles and hence the accuracy with which ΔD_{NH} can be determined,[17] further simulations with the same parameters as for the simulations in Figure 8 but (i) with k_{ex} varied between 200 and 1500 s^{-1}, (ii) with p_E set to 3%, or (iii) with $\Delta\varpi_{N,GE}$ varied between 0.5 and 2 ppm produced error profiles that are similar to those shown here.

Concluding Remarks

We have presented a detailed analysis of the effects of strong $^1H^N-^1H^N$ dipolar couplings on ^{15}N TR/AT CPMG relaxation dispersion experiments and how such effects influence extracted ΔD_{NH} values. On the basis of these results, we recommend the following procedure to minimize systematic errors in measured excited-state $^1H^N-^{15}N$ RDCs to below 1−2 Hz.

(i) Use relatively mild alignment conditions such that ground-state $^1H^N-^{15}N$ RDCs are within approximately ±20−25 Hz so that $^1H^N-^1H^N$ dipolar couplings will (very likely) be less than 15 Hz.

(ii) A priori, identify residues that will be affected by strong coupling from $^1H^N$ chemical shifts and predicted $^1H^N-^1H^N$ RDCs that are obtained on the basis of alignment parameters generated from fits of the experimental ground-state $^1H^N-^{15}N$ RDCs to the ground-state structure. Simulations have shown that strong coupling effects in the excited state have minimal effect because this state is populated to only a few percent.

(iii) Residue pairs that have predicted $^1H^N-^1H^N$ couplings <5 Hz can be included in the analysis, independent of $^1H^N$ chemical shift offsets.

(iv) Residue pairs with predicted $^1H^N-^1H^N$ RDC values $\approx$10 Hz (15−20 Hz) and with $^1H^N$ chemical shifts within 0.1 (0.15) ppm should be discarded from the analysis. In some cases, especially when experimental errors are significant, the goodness of fit criteria cannot be used to establish whether strong coupling effects are influencing extracted $^1H^N-^{15}N$ RDC values since fits can appear to be satisfactory.

(v) Residue pairs that have predicted $^1H^N-^1H^N$ RDC values between 5 and 10 Hz with $^1H^N$ chemical shifts within 0.05 ppm should be discarded from the analysis.

There have been at most one or two residue pairs in each of the three or four 60−70-residue protein domains that we have examined to date with contamination from strong coupling effects. The guidelines provided above ensure that robust values of couplings can be extracted, leading to accurate descriptions

of excited protein states and ultimately insight into how these invisible conformers relate to biological function.

Acknowledgment. We thank Drs. D. F. Hansen, P. Vallurupalli, A. Velyvis, and G. Bouvignies (University of Toronto) for helpful discussion. H.v.I. thanks the Niels Stensen Foundation for a postdoctoral fellowship. This work was supported by a grant from the Canadian Institutes of Health Research. L.E.K. holds a Canada Research Chair in Biochemistry.

References and Notes

(1) Eisenmesser, E. Z.; Millet, O.; Labeikovsky, W.; Korzhnev, D. M.; Wolf-Watz, M.; Bosco, D. A.; Skalicky, J. J.; Kay, L. E.; Kern, D. *Nature* **2005**, *438*, 117–121.

(2) Boehr, D. D.; Mcelheny, D.; Dyson, H. J.; Wright, P. E. *Science* **2006**, *313*, 1638–1642.

(3) Korzhnev, D. M.; Salvatella, X.; Vendruscolo, M.; Di Nardo, A. A.; Davidson, A. R.; Dobson, C. M.; Kay, L. E. *Nature* **2004**, *430*, 586–590.

(4) Mulder, F. A.; Mittermaier, A.; Hon, B.; Dahlquist, F. W.; Kay, L. E. *Nat. Struct. Biol.* **2001**, *8*, 932–935.

(5) Sugase, K.; Dyson, H. J.; Wright, P. E. *Nature* **2007**, *447*, 1021–1025.

(6) Palmer, A. G.; Kroenke, C. D.; Loria, J. P. *Methods Enzymol.* **2001**, *339*, 204–238.

(7) Carr, H. Y.; Purcell, E. M. *Phys. Rev.* **1954**, *94*, 630–638.

(8) Meiboom, S.; Gill, D. *Rev. Sci. Instrum.* **1958**, *29*, 688–691.

(9) Loria, J. P.; Rance, M.; Palmer, A. G. *J. Am. Chem. Soc.* **1999**, *121*, 2331–2332.

(10) Tollinger, M.; Skrynnikov, N. R.; Mulder, F. A.; Forman-Kay, J. D.; Kay, L. E. *J. Am. Chem. Soc.* **2001**, *123*, 11341–11352.

(11) Korzhnev, D. M.; Kay, L. E. *Acc. Chem. Res.* **2008**, *41*, 442–451.

(12) Hansen, D. F.; Vallurupalli, P.; Lundström, P.; Neudecker, P.; Kay, L. E. *J. Am. Chem. Soc.* **2008**, *130*, 2667–2675.

(13) Lundström, P.; Hansen, D. F.; Kay, L. E. *J. Biomol. NMR* **2008**, *42*, 35–47.

(14) Ishima, R.; Baber, J.; Louis, J. M.; Torchia, D. A. *J. Biomol. NMR* **2004**, *29*, 187–198.

(15) Ishima, R.; Torchia, D. A. *J. Biomol. NMR* **2003**, *25*, 243–248.

(16) Lundström, P.; Hansen, D. F.; Vallurupalli, P.; Kay, L. E. *J. Am. Chem. Soc.* **2009**, *131*, 1915–1926.

(17) Vallurupalli, P.; Hansen, D. F.; Stollar, E.; Meirovitch, E.; Kay, L. E. *Proc. Natl. Acad. Sci. U.S.A.* **2007**, *104*, 18473–18477.

(18) Hansen, D. F.; Vallurupalli, P.; Kay, L. E. *J. Am. Chem. Soc.* **2008**, *130*, 8397–8405.

(19) Igumenova, T. I.; Brath, U.; Akke, M.; Palmer, A. G. *J. Am. Chem. Soc.* **2007**, *129*, 13396–13397.

(20) Tjandra, N.; Bax, A. *Science* **1997**, *278*, 1111–1114.

(21) Tolman, J. R.; Flanagan, J. M.; Kennedy, M. A.; Prestegard, J. H. *Proc. Natl. Acad. Sci. U.S.A.* **1995**, *92*, 9279–9283.

(22) Hansen, D. F.; Vallurupalli, P.; Kay, L. E. *J. Biomol. NMR* **2008**, *41*, 113–120.

(23) Kumar, A.; Ernst, R. R. *J. Magn. Reson.* **1976**, *24*, 425–447.

(24) Mulder, F. A.; Hon, B.; Mittermaier, A.; Dahlquist, F. W.; Kay, L. E. *J. Am. Chem. Soc.* **2002**, *124*, 1443–1451.

(25) Lundström, P.; Teilum, K.; Carstensen, T.; Bezsonova, I.; Wiesner, S.; Hansen, D. F.; Religa, T. L.; Akke, M.; Kay, L. E. *J. Biomol. NMR* **2007**, *38*, 199–212.

(26) Vallurupalli, P.; Scott, L.; Williamson, J. R.; Kay, L. E. *J. Biomol. NMR* **2007**, *38*, 41–46.

(27) Wu, Z. R.; Bax, A. *J. Am. Chem. Soc.* **2002**, *124*, 9672–9673.

(28) Allen, M.; Friedler, A.; Schon, O.; Bycroft, M. *J. Mol. Biol.* **2002**, *323*, 411–416.

(29) Jemth, P.; Gianni, S.; Day, R.; Li, B.; Johnson, C. M.; Daggett, V.; Fersht, A. R. *Proc. Natl. Acad. Sci. U.S.A.* **2004**, *101*, 6450–6455.

(30) Jemth, P.; Day, R.; Gianni, S.; Khan, F.; Allen, M.; Daggett, V.; Fersht, A. R. *J. Mol. Biol.* **2005**, *350*, 363–378.

(31) Korzhnev, D. M.; Religa, T. L.; Lundström, P.; Fersht, A. R.; Kay, L. E. *J. Mol. Biol.* **2007**, *372*, 497–512.

(32) Hansen, D. F.; Vallurupalli, P.; Kay, L. E. *J. Phys. Chem. B* **2008**, *112*, 5898–5904.

(33) Ruckert, M.; Otting, G. *J. Am. Chem. Soc.* **2000**, *122*, 7793–7797.

(34) Valafar, H.; Prestegard, J. H. *J. Magn. Reson.* **2004**, *167*, 228–241.

(35) Cavanagh, J.; Fairbrother, W. J.; Palmer, A. G.; Skelton, N. J.; Rance, M. *Protein NMR Spectroscopy: Principles and Practice*, 2nd ed.; Academic Press: New York, 2007.

(36) Mcconnell, H. M. *J. Chem. Phys.* **1958**, *28*, 430–431.

(37) Helgstrand, M.; Härd, T.; Allard, P. *J. Biomol. NMR* **2000**, *18*, 49–63.

(38) Abragam, A. *The Principles of Nuclear Magnetism*; Oxford University Press: London, 1961.

(39) Loria, J. P.; Rance, M.; Palmer, A. G. *J. Biomol. NMR* **1999**, *15*, 151–155.

(40) Palmer, A. G.; Skelton, N. J.; Chazin, W. J.; Wright, P. E.; Rance, M. *Mol. Phys.* **1992**, *75*, 699–711.

JP902793Y